

# JGR Solid Earth

## RESEARCH ARTICLE

10.1029/2020JB020329

# Inverse Migration of Seismicity Quiescence During the 2019 Ridgecrest Sequence

D. Marsan<sup>1</sup>  and Z. E. Ross<sup>2</sup> 

<sup>1</sup>ISTerre, Université Savoie Mont-Blanc, CNRS, IRD, IFSTTAR, Le Bourget-du-Lac, France, <sup>2</sup>Seismological Laboratory, California Institute of Technology, Pasadena, CA, USA

### Key Points:

- The 2019 Ridgecrest sequence is characterized by a seismicity shutdown following the second (magnitude 7.1) shock
- This shutdown occurs immediately after the M7.1 shock at the tips of the main M6.4 fault, and then migrates toward its center
- The use of template matching data and stochastic modeling allows for an improved characterization of earthquake rate changes

### Supporting Information:

- Supporting Information S1

### Correspondence to:

D. Marsan,  
[david.marsan@univ-savoie.fr](mailto:david.marsan@univ-savoie.fr)

### Citation:

Marsan, D., & Ross, Z. E. (2021). Inverse migration of seismicity quiescence during the 2019 Ridgecrest sequence. *Journal of Geophysical Research: Solid Earth*, 126, e2020JB020329. <https://doi.org/10.1029/2020JB020329>

Received 2 JUN 2020

Accepted 16 OCT 2020

**Abstract** Seismicity quiescences are best observed during sequences with multiple mainshocks and often emerge with some delay after an initial phase of aftershock triggering. The mechanisms controlling this delay are poorly understood, due to a lack of systematic and precise estimation of the duration of the triggering phase which is made complicated by the rapidly changing magnitude of completeness after the mainshock. Here, we analyze how such a delayed quiescence developed during the 2019 Ridgecrest (California) sequence, using a refined earthquake data set obtained by template matching and relative relocation. A method that allows estimating the aftershock occurrence rate after correcting for the change in detection (completeness magnitude) is applied. We find that an immediate seismicity shutdown was triggered by the second (M7.1) mainshock at the tips of the north-east trending cross-cut fault that hosted most of the slip of the first (M6.4) mainshock. This shutdown progressed toward the central part of this fault over the following days. The overall shutdown of the aftershock sequence of the M6.4 by the M7.1 rupture is consistent with static Coulomb stress modeling. This inverse migration is a unique observation, best explained by an enhanced spatial stress change variability in this central part where the cross-cut fault intersects the main fault of the M7.1 shock, hence a strongly damaged zone there. This further confirms previous observations of an enhanced structural disorder in this central part of the cross fault, showing that structural disorder has a first-order control on the seismicity dynamics at the scale of days.

## 1. Introduction

The existence of stress shadows following earthquakes has been postulated for more than 3 decades (Harris & Simpson 1996, 1998, 2002), but their relevance when looking at time scale of days to months after the mainshock has remained questionable until more recently. Recent observations have focused on seismic activity, which, in a stress shadow, is expected to decrease. However, other factors and processes can act to either reduce or delay this suppressing effect, in particular: additional stress steps by subsequent earthquakes (Meier et al., 2014), dynamic triggering (Felzer & Brodsky, 2006), nonuniformity of the stress field and complex fault geometries (Helmstetter & Shaw, 2006; Marsan, 2006), stress-induced fluid intrusions (Yoshida & Hasegawa, 2018). On the contrary, increase of activity after a mainshock is an ubiquitous feature, taking the form of aftershock sequences following the well-established Omori's law (Omori, 1895), as well as remotely triggered earthquakes potentially very far from the causative rupture (Pollitz et al., 2012). This observational bias toward triggering has initially led some authors to doubt the existence of seismicity quiescences (Felzer & Brodsky, 2005; Mallman & Zoback, 2007), others arguing that they play an anecdotal role in the overall earthquake rate change budget (Marsan, 2003). However, observations of seismicity quiescences have since then accumulated, mostly for earthquake doublets (Daniel et al., 2006, 2008; Kroll et al., 2017; Ma et al., 2005; Marsan & Daniel, 2007; Marsan & Nalbant, 2005; Meng & Peng, 2014; Meng et al., 2013; Sevilgen et al., 2012; Toda & Stein 2002, 2003; Toda et al., 2012; Woessner et al., 2004; Wyss & Wiemer, 2000) or magma-induced activity (Dieterich and Okubo, 1996; Dieterich et al., 2000; Green et al., 2015; Maccafferri et al., 2013), both types of systems being characterized by abundant seismicity prior to the appearance of the stress shadow.

A common observation is that quiescences do not start immediately after the mainshock, and are even sometimes preceded by a phase of initial triggering, the delay varying from days (e.g., Toda & Stein, 2003; Woessner et al., 2004) to months (e.g., Ma et al., 2005; Toda & Stein, 2002). Quasiinstantaneous shutdowns were found by Meng et al. (2013), Green et al. (2015) and Kroll et al. (2017), but are particularly challenging to observe for several reasons: (1) the computation of a decrease in seismicity rate requires smooth-

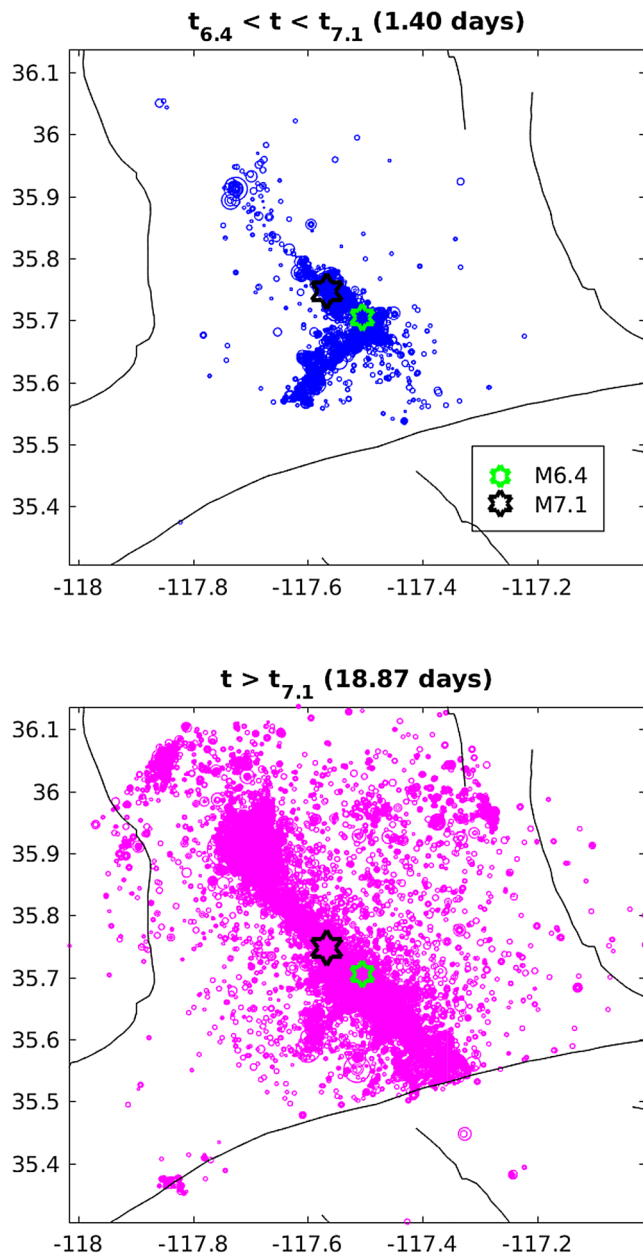


**Figure 1.** Map of the zone studied and earthquake activity (QTM data set). Top: 1.4 days of activity following the M6.4 mainshock. Bottom: 18.87 days of activity after the M7.1 mainshock. QTM, Quake Template Matching.

ing, potentially over an extended period of time if the prior activity is too sparse (Marsan & Nalbant, 2005); (2) the reporting of earthquakes is not stationary after large mainshocks, resulting in many earthquakes being missed out that would normally be reported at more quiet times; (3) the decrease in activity can sometimes be dated to start prior to the mainshock (Marsan & Nalbant, 2005; Meng et al., 2013), raising doubts as to the exact role of the mainshock in causing this decrease.

We here analyze the Ridgecrest sequence that took place in California in 2019. Two large shocks of moment magnitudes 6.4 and 7.1 occurred on July 4 and 6, with about 34 h between the two. A remarkable feature is that the first mainshock ruptured both a NE-SW left-lateral (the Salt Wells Valley Fault or SWVF, DuRoss et al., 2020) and a nearly orthogonal NW-SE right-lateral strike-slip faults, the second mainshock then resuming the rupture on this second structure past a supposedly resisting but eroding asperity (Chen et al., 2020; Liu et al., 2019; Ross et al., 2019). Abundant seismicity followed both mainshocks and detailed analyses of this activity have revealed a complex zone of deformation with many small faults cross-cutting the main NW-SE Paxton Ranch fault (Ross et al., 2019). It has been argued that the SWVF was shut down by the M7.1 mainshock, in coherence with static stress modeling (Toda & Stein, 2019). Traditionally, seismicity rate changes caused by a mainshock are computed by comparing the rate of seismicity after the mainshock with that before, after selecting earthquakes above a threshold (completeness) magnitude (Marsan, 2003). In the present case, the robustness of this type of analysis is questionable given the short (34 h) delay between the two shocks and the fact that rapid changes in completeness magnitude interfere with the estimation of seismicity rates. We show in section A of the Supplementary Material that this approach indeed cannot resolve whether the aftershock sequence of the first mainshock was affected by the occurrence of the M7.1 shock. We here make use of the improved Quake Template Matching (QTM) catalog of Ross et al. (2019) to investigate the role of the second (M7.1) mainshock in altering the aftershock sequence of the initial M6.4 shock. To do so, we develop a method that optimizes the available information, reducing the volume of data discarded by imposing a large completeness magnitude, hence allowing to keep as large a number of earthquakes as possible to better estimate the seismicity rates and their corresponding changes.

## 2. Data

We study the seismic activity starting at the time of the M6.4 mainshock (2019/7/4, 17:34:17) and finishing 18.87 days after the M7.1 mainshock, hence a 20.26 day interval, in the region bounded by (−118.0160, −117.0115) in longitude and (35.3053, 36.1370) in latitude, that covers

the aftershock zone of the first mainshock, cf. Figure 1. The SCSN catalog counts 18,200 earthquakes for this area and time interval. We use the QTM catalog to complement these data (Ross et al., 2019), the whole data set being made up of 111,537 earthquakes in total. For the sake of comparison, a specific analysis of the SCSN data alone is detailed in Text S1.

The observed rate of occurrence is constant over these 20.20 days, even though the two mainshocks trigger aftershock sequences, cf. Figure 2. This is due to the high rate of earthquakes during this sequence, and the ability of the Template Matching method to detect small events: on average, the method can always find at least one occurrence in every 15 s, and among those detections only keeps one. Whether a poten-

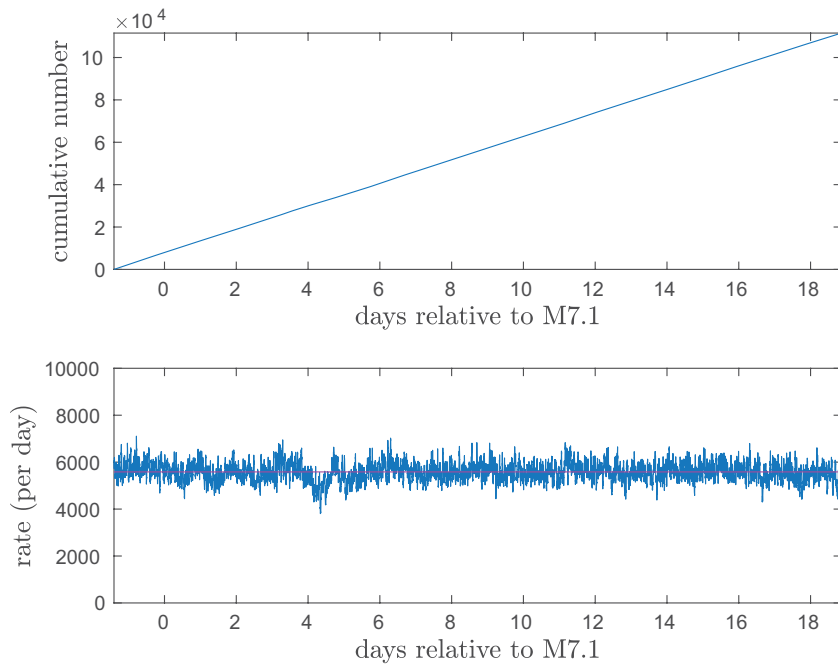


**Figure 2.** (Top) cumulative and (bottom) rate of earthquakes smoothed over 100 successive earthquakes. The mean rate is 5,584 per day (magenta line), corresponding to one earthquake every 15 s on average.

tial detection is kept or not depends on a number of factors (e.g., correlations with the template waveforms, which values depend on the magnitude of the detected earthquake, the proximity to the seismic stations, the frequency content of the template waveforms, etc.), and on the parameterization of the method. Here, we will postulate that the selection is controlled by the magnitude of the detected earthquake, a higher magnitude implying a larger wave amplitude, hence a better signal-to-noise ratio, therefore a larger correlation coefficient. We will show in Section 3.1 that this assumption can be a posteriori validated. Moreover, it allows for a simplified correction of the rapid variations in magnitude completeness, as is now detailed. We emphasize that our assumption is only a working hypothesis (i) that seems realistic given the factual observation that the rate is at first order constant during 20 days (Figure 2), (ii) that can be validated a posteriori, cf. Section 3.1, and (iii) that, quite importantly, can be exploited to develop an efficient strategy for correcting for time-varying completeness issues. There is however no straightforward proof based solely on the use of the template matching method that such a constant rate should naturally emerge from this complex identification/selection algorithm.

### 3. Methods

We here detail how the rate of earthquakes can be estimated with much greater accuracy than with more traditional methods that impose a strict magnitude of completeness. The lack of resolution of the latter is demonstrated in the Supporting Information, both with the actual (Section A) and synthetic data (Section C).

#### 3.1. Modeling the Time-Varying Probability of Detection

Because seismic noise becomes strong immediately after a mainshock (overlap of coda waves, of nearly coincidental aftershocks, etc.), our capacity to isolate phases from overlapping waveforms, and hence to detect earthquakes, is lowered, and only large earthquakes can be identified and localized early in

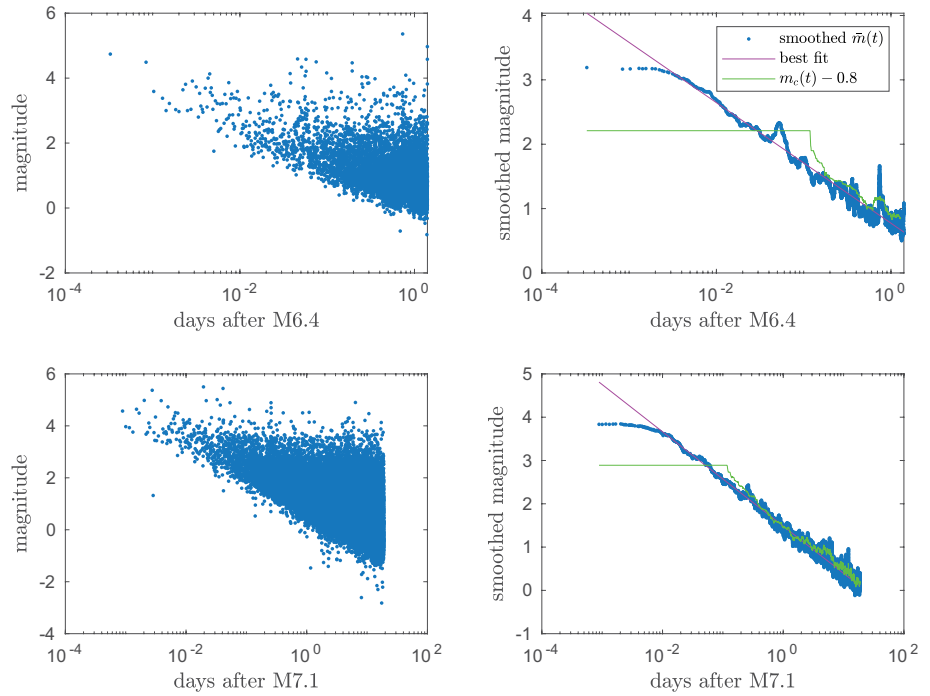


**Figure 3.** Magnitudes (left) and smoothed magnitudes (right) versus time, for each sequence (we here stop the sequence of the first mainshock at the time of occurrence of the second mainshock, hence after 1.4 days). The smoothing is computed on 100 successive earthquakes. Magenta: best linear fit in  $\ln(t - t_{MS})$ . Green:  $m_c(t) - 0.8$ , with  $m_c$  estimated using Hainzl's method (Hainzl, 2016a). The departure of  $m_c(t) - 0.8$  with  $\bar{m}(t)$  is mostly caused by the smoothing procedure, which is different between the two approaches.

the aftershock sequence. As a consequence, the magnitudes of the listed earthquakes depend on the time elapsed since the last mainshock, cf. Figure 3. In order to describe and quantify this dependence with time, we smooth magnitudes from successive earthquakes, separately for the two aftershock sequences. A decay with the logarithm of time is found:  $\bar{m}_{mod}(t) = -0.39 \ln(t - t_{6.4}) + 0.79$  and  $\bar{m}_{mod}(t) = -0.47 \ln(t - t_{7.1}) + 1.48$  for the M6.4 and the M7.1 sequences respectively, where time is measured in days (Figure 3). This is consistent with the observation of Helmstetter et al. (2006) following California mainshocks, who found that the completeness magnitude evolves as  $m_c(t) = -0.32 \ln(t - t_{MS}) + m_{MS} - 5$ , where  $t_{MS}$  and  $m_{MS}$  are the time and magnitude of the mainshock. In order to compare our observation (decrease of the smoothed magnitude  $\bar{m}$  with time) with theirs (decrease of the completeness magnitude  $m_c$  with time), we use the fact that an earthquake with magnitude  $m = \bar{m}_{mod}(t)$  has a 0.55 probability of being detected, this probability becoming 0.9 when  $m = \bar{m}_{mod}(t) + 0.80$ , in the case of our data set (see Text S2 for a derivation of these values). Assuming that  $m_c$  corresponds to a fixed detection probability (e.g., 0.9), it implies that the (i) the slope of  $m_c(t)$  with  $\ln(t - t_{MS})$  is equal to that of  $\bar{m}_{mod}(t)$ , and (ii) that the proposed direct proportionality of  $m_c(t)$  with  $m_{MS}$  should also be found for  $\bar{m}_{mod}(t)$ , as is indeed the case. We verify (i) by running the algorithm of Hainzl (2016a), which allows for estimation of  $m_c(t)$  during aftershock sequences. We fix Hainzl's  $p_c$  (probability to detect an  $m > m_c$  earthquake) to 0.9,  $\Delta t$  (screening time) to 15 s, and compute the rate over  $N = 100$  successive earthquakes. Given this value of  $p_c$ , subtracting 0.80 to the estimated  $m_c(t)$  should yield our  $\bar{m}_{mod}(t)$ , as is indeed found, see Figure 3.

We next define the incremental magnitude of an earthquake  $\{t_i, m_i\}$  as  $\delta m_i = m_i - \bar{m}_{mod}(t_i)$ . The distribution of  $\delta m$  is now to first order independent of time, and corresponds to a Gutenberg-Richter law modulated by a detection probability  $q(\delta m)$ , both components being individually independent of time. Recalling our working hypothesis that, on average, there is one earthquake every 15 s, and that this detected earthquake is the biggest in magnitude among all potential detections during these 15 s, we show

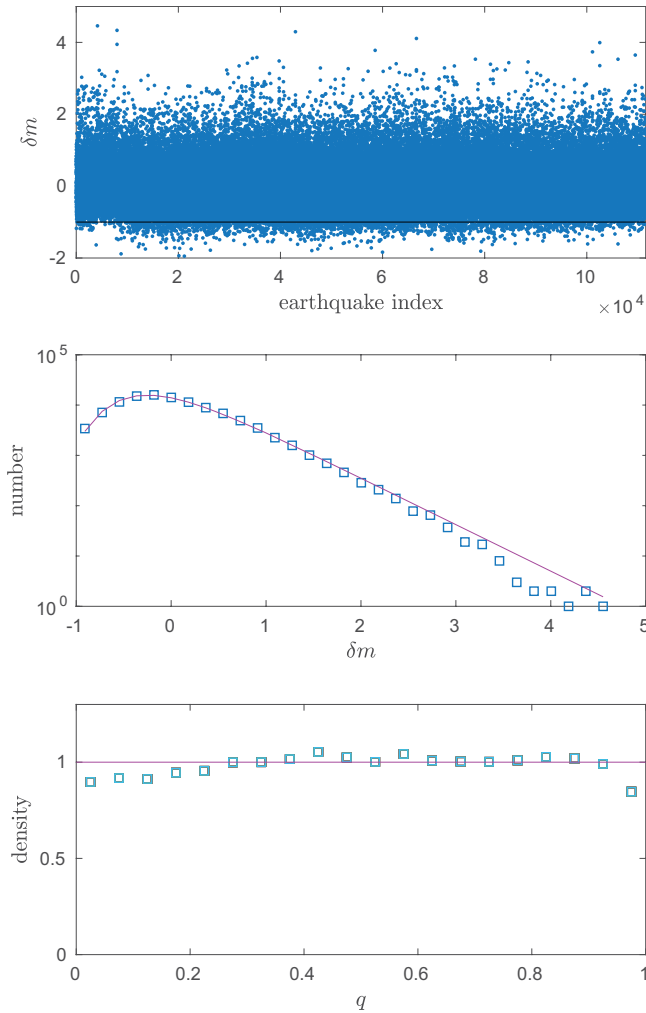


**Figure 4.** (Top) incremental magnitude versus earthquake index. We fit this distribution for  $\delta m \geq -1$  values (black line) with a Gutenberg-Richter law modulated by a Gumbel detection function  $q(\delta m)$  (in magenta), middle graph. (Bottom) distribution of  $q_i$  values, and the expected uniform density (in magenta).

in Text S2 (see also Hainzl, 2016b) that  $q(\delta m)$  should then follow a Gumbel distribution  $\ln q(\delta m) = -\exp(-\beta(\delta m - \mu))$  with  $\beta = b \ln 10$ ,  $b$  denoting the  $b$ -value of the Gutenberg-Richter law,  $\mu = \overline{\delta m} - 0.577 / \beta$  and  $\overline{\delta m} = 0.007$  the mean of the 111,537 incremental magnitudes. We use this model to fit the distribution of  $\delta m$  for  $\delta m > m_{\min}$  with  $m_{\min} = -1$  (hence discarding 1.6% of all earthquakes with anomalously low incremental magnitudes, all of them but one coming from the QTM data set), see Figure 4. We find that  $\beta = 2.14$ , or equivalently  $b = 0.92$ . The validity of our working hypothesis is tested by checking that the  $\{q_i\}$  values, defined as  $\ln q_i = -\exp(-\beta(m_i - \overline{m}_{\text{mod}}(t_i) - \mu))$ , are distributed according to a uniform law, as is expected (cf. Text S2).

### 3.2. Corrected Earthquake Rates

Given our detection model, we then correct the earthquake rates for missed (undetected) earthquakes. We show in Text S2 that the observed rate  $\lambda_{\text{obs}}(t)$ , which is to first-order constant with time, must be normalized by a correction factor  $\pi = e^{-\beta x} \{1 - \exp(-e^{-\beta x})\}$  with  $x = \mu + \overline{m}_{\text{mod}} - m_{\min}$ . The corrected rate is then  $\lambda(t) = \lambda_{\text{obs}}(t)/\pi(t)$ . This is true for any chosen area, i.e., we must apply the same correction with the same  $\pi(t)$  function to the rate observed for any (however small) area. The observed rate  $\lambda_{\text{obs}}(t)$  is simply equal to  $\frac{N-1}{\delta t(t)}$ , where  $N$  is a smoothing parameter and  $\delta t(t)$  is the duration between the first and the last of the  $N$  earthquakes closest to time  $t$  occurring in the studied area.

Figure 5 shows the corrected rate  $\lambda$  using  $N = 10$ , for the whole geographical box. We separately compute  $\lambda$  for two time intervals  $t_{6.4} < t < t_{7.1}$  and  $t > t_{7.1}$  since  $\overline{m}_{\text{mod}}(t)$  hence  $\pi(t)$  are also modeled separately. Even though the observed rates are constant, the corrected rates now follow an Omori's law, with a  $p$ -exponent equals to 0.87 and 1.00, respectively, for the two  $t_{6.4} < t < t_{7.1}$  and  $t > t_{7.1}$  sequences.

### 3.3. Changes in Earthquake Rate

In order to estimate how the aftershock sequence of the M6.4 is affected by the occurrence of the M7.1, we model for any given area the local corrected rate  $\lambda(t < t_{7.1})$ , extrapolate this model to  $t > t_{7.1}$ , and compare this extrapolation to the real corrected rate. This can be done for any target time interval. We model the corrected rate as the sum of two Omori's laws initiated by the M6.4 and by its strongest aftershock (a magnitude 5.3 earthquake that occurred 17 h after the first mainshock):  $\lambda_{\text{mod}}(t) = K_{6.4}(t - t_{6.4})^{-p} + K_{5.3}(t - t_{5.3})^{-p}$ , which assumes a negligible cut-off time scale (i.e., the "c"-value of both Omori's laws is set to 0). We find the best  $p$ ,  $K_{6.4}$ , and  $K_{5.3}$  that fit the data, using a simple least-square fit of the logarithm of the rate. We compute (i) the normalized variance of the residuals  $v = \frac{\text{var}(\ln \lambda - \ln \lambda_{\text{mod}})}{\text{var}(\ln \lambda)}$  for  $t_{6.4} < t < t_{7.1}$  in order to assess the quality of the model ( $v$  should be close to 0 for a good model), and (ii) the rate change  $\rho$  as the mean of  $\log_{10} \lambda_{\text{mod}} - \log_{10} \lambda$  for  $\lambda_{\text{mod}}$  and the corrected  $\lambda$  in the target time interval, so that  $\lambda = \lambda_{\text{mod}} 10^\rho$ . We test our method in Text S3 by simulating earthquake catalogs that mimic the Ridgecrest sequence, and for which we impose a (known) rate change. We find that, for areas that contain on average about 200 detected earthquakes within the initial 1.4 days (our analysis will consider comparable numbers), the uncertainty on the estimated  $\rho$  is 0.19.

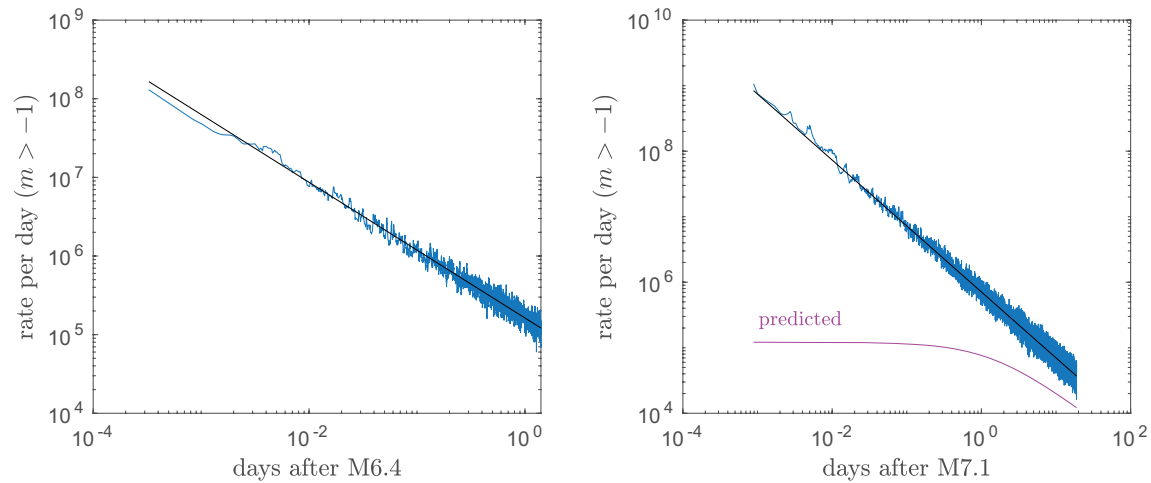


**Figure 5.** Corrected rate of  $m \geq -1$  earthquakes per day following the M6.4 (left) and the M7.1 (right) mainshocks. Black lines: best log-log fits, giving Omori's law exponents  $p = 0.87$  and  $p = 1.00$  respectively. The rate predicted by extrapolating the  $t < t_{7.1}$  rate to  $t > t_{7.1}$  is shown in magenta. The M7.1 clearly triggered extra activity when considering the whole geographical box.

## 4. Results

### 4.1. Rate Changes

We select the geographical areas by considering the 7,995 earthquakes that occurred between the M6.4 and the M7.1, and for each of those select the 3D volume that encompass the  $N = 400$  closest  $t_{6.4} < t < t_{7.1}$  earthquakes. Figure 6 shows the obtained maps of  $\nu$  and  $\rho$ ; Figure 7 displays the rates for six sample locations (labeled A–F on Figure 6). Both positive (triggering) and negative (quiescence) rate changes are observed, with most notably the activity on the 25 km-long cross-fault being shutdown, and more significantly so at the tips (locations B and F). The area near the M5.3 aftershock (location A) also displays a decrease in rate, but it must be noted that the fit, while of good quality ( $\nu = 0.27$  for A), yields an Omori's law  $p$ -value of 0.45 which is anomalously low; this could indicate that the 0.7 day-long interval between the M5.3 and the M7.1 is not long enough to allow for a robust modeling of the rate prior to the M7.1 mainshock. This area marks the arrest of the M6.4 coseismic rupture to the north-west. This resisting asperity eventually broke with a succession of M4 to M5.3 earthquakes in the following 1.4 days, after which the rupture resumed just past this barrier, the M7.1 epicenter being located just after it (Ross et al., 2019). An alternative explanation is thus that the low  $p$ -value of 0.45 is real and indeed characterizes a slowly eroding asperity, in which case the quiescence found for the area around location A is also real.

Previous studies of doublets have already found that both triggering and quiescence can be observed, but that triggering dominates when considering the whole rupture zone of the first mainshock. In fact, we are not aware of any previous observation of a whole aftershock zone being seismically inhibited by a subsequent mainshock. Our results of Figure 6 suggest that the M6.4 rupture zone was overall shutdown by the M7.1 shock. We thus specifically focus on this rupture zone. To do so, we use the fact that, in the QTM catalog, template earthquakes can have more than one occurrence. These newly detected events are estimated to originate within a  $100 \times 100 \times 350$  m volume containing the original template event (Ross et al., 2019). Selecting all newly detected (QTM) earthquakes that have at least two occurrences between the M6.4 and the M7.1 is therefore equivalent to sampling the M6.4 aftershock zone with a  $\approx 100$ – $350$  m resolution, this sampling naturally highlighting the most active parts of the fault. We thus select these earthquakes, complement them with extra template detections listed in the QTM catalog that took place after the M7.1 mainshock, and compare how the extrapolated, corrected rate (based on preM7.1 occurrences) differs from the corrected, postM7.1 rate (Figure 8). A clear shutdown is found after an initial 7 h long period of triggering, the rate being divided by a factor of 5 for the 18.87 day long target interval. We obtain similar results by simply selecting all postM7.1 earthquakes that are within 100–300 m of a preM7.1 earthquake: the rate is divided by a factor of 7 (at 100 m) to 2 (at 300 m). This proves that in sequences of two (or more) successive mainshocks, the seismic rate history can be far more complex than the simple superposition of two (independent) aftershock sequence: here, the M7.1 significantly shuts down the M6.4 aftershock sequence.

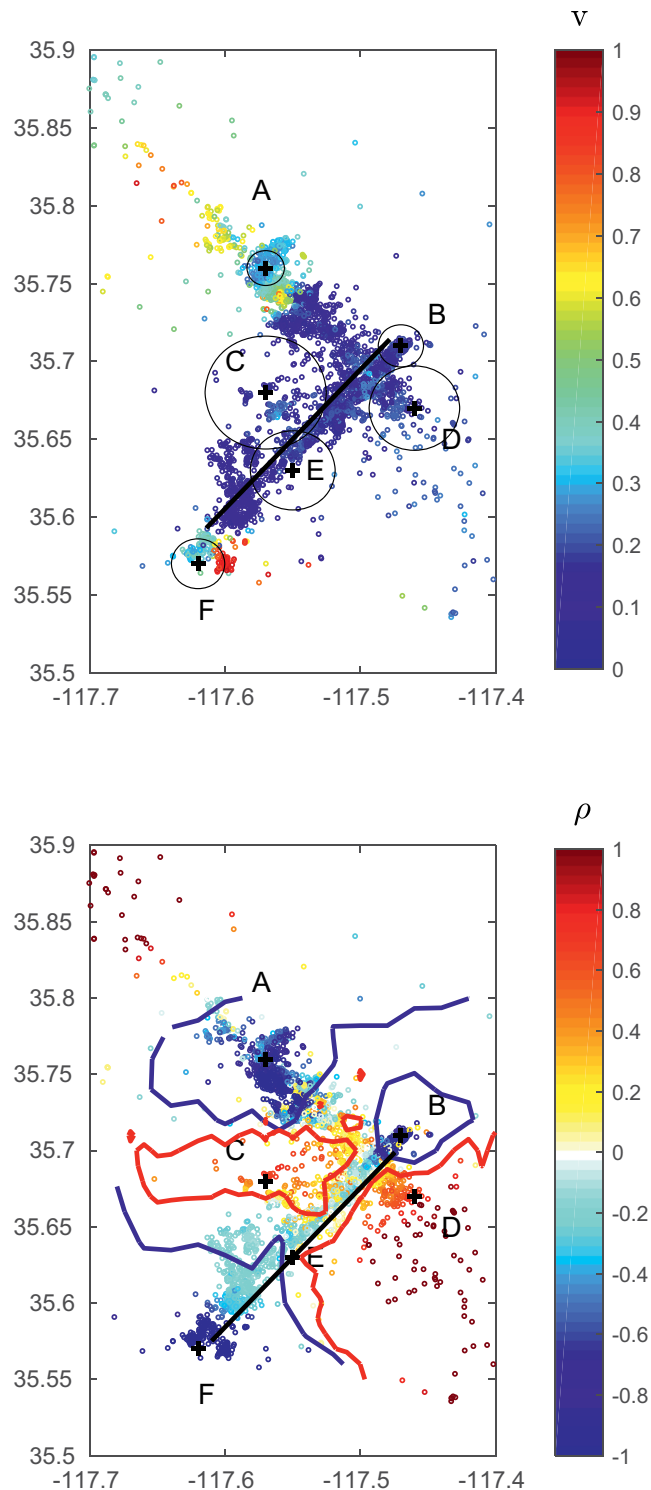


**Figure 6.** Normalized variance  $v$  (top) and rate change  $\rho$  (bottom) following the M7.1 mainshock, for  $N = 400$  and the  $t_{7.1} < t < t_{7.1} + 18.87$  days target interval. The two quantities  $v$  and  $\rho$  are only estimated at the locations of the 7,995 aftershocks occurring between the two mainshocks, cf. main text. Values near 0 for  $v$  indicate that the modeling of the rate time series is good;  $\rho$  is the ratio of the rate change in log 10. The thick red and blue lines show the  $\rho > 0.2$  and  $\rho < -0.2$  contours. Locations A–F are selected locations for which the rate time series are shown in Figure 7. The high- $v$  value zone near F, while effectively badly modeled, is really affected by a clear activity shutdown, as confirmed by visually inspecting the time series, cf. Figure 7 (F). The black circles on the top map show the radii encompassing the  $N = 400$  closest earthquakes to locations A–F. The B–F segment corresponding to the cross fault (SWV Fault) is displayed (thick black line). SWV, Salt Wells Valley.

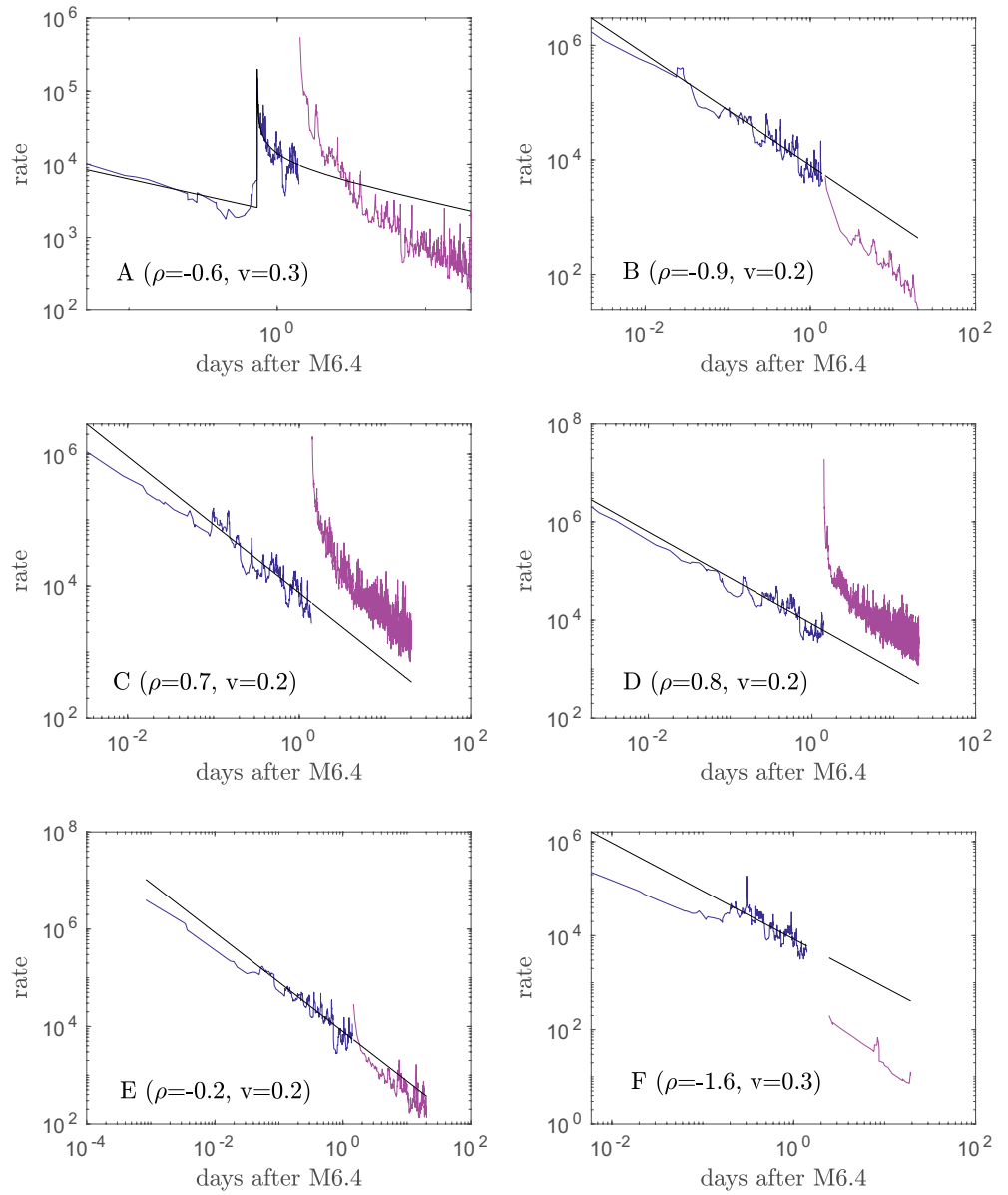


**Figure 7.** Rates of  $m \geq -1$  earthquakes (per day) for the six locations A-F of Figure 6. Blue and magenta: corrected rate prior to and after the M7.1 mainshock, respectively. Black: modeled rate fitted to the blue rate and extrapolated to the post-M7.1 interval. The rate change is estimated by computing the magenta and the black rates, and averaging this ratio over the 18.87 days after the M7.1.

#### 4.2. Coulomb Stress Modeling

We compute the change in Coulomb stress caused by the M7.1 mainshock (Toda et al., 2011). To do so, we use the slip model of Ross et al. (2019), assume a friction coefficient of 0.4, and use for the target fault geometry the same geometry as the SWVF: A left-lateral vertical strike-slip fault striking at  $221^\circ$ . This geometry is favorably oriented for a regional stress field with a vertical  $\sigma_3$  axis, and  $\sigma_1$  oriented at  $7^\circ$ NE, so that the Coulomb stress change map we obtain is very similar (at the regional scale) to the one found by Rollins et al. (2019) using optimally oriented strike-slip faults. The fault geometry used by Ross et al. (2019) has the main fault dipping  $60^\circ$  to the northeast across transect B-F. Here, the cross-section displays a (strong) negative stress change, with the exception of a central portion at the intersection of the main M7.1 rupture plane, see Figure 9. Unresolved slip heterogeneity would affect this central portion, so that the computed

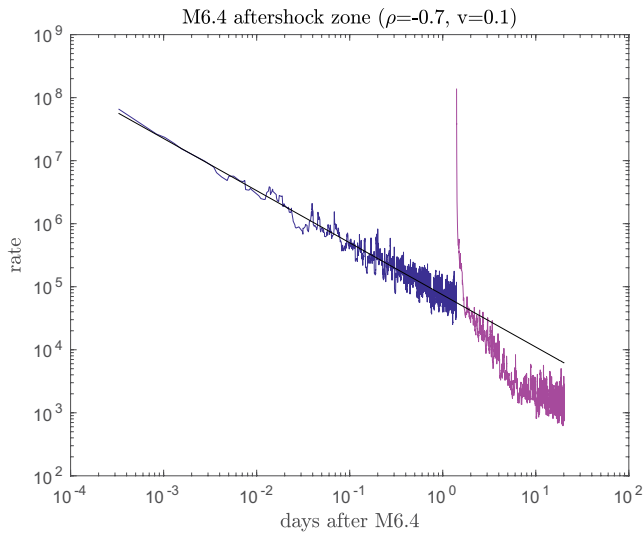


**Figure 8.** Rates of  $m \geq -1$  earthquakes (per day) for the whole aftershock zone of the M6.4 mainshock, using multiple occurrences of template earthquakes. Blue and magenta: corrected rate prior to and after the M7.1 mainshock, respectively. Black: modeled rate fitted to the blue rate and extrapolated to the post-M7.1 interval. The rate change is estimated by comparing the magenta and black rates, averaged over the 18.87 days after the M7.1. Triggering is observed for the first 7 h after the M7.1, followed by a quiescence (rate divided by a factor of 5).

stress there must be considered with caution. The overall negative stress change is fully consistent with the observed quiescence along the cross fault (Figure 9, right bottom graph), and when considering the rupture zone of the M6.4 as a whole (Figure 8). The positive stress change in the central part is also consistent with the observed triggering below 7 km in this zone.

### 4.3. Delayed Quiescence and Migration

The initial triggering observed during the first 7 h (Figure 8) is obtained by averaging over the whole M6.4 rupture zone, hence hiding local differences in how the quiescence is delayed. In particular, for locations B and F, the observed rate is always less than the extrapolated rate, for all the post-M7.1 earthquakes in the selected area. We thus analyze how the delay with which the quiescence starts varies along the cross fault (keeping all earthquakes within 2 km of the B-F transect), see Figure 10. The observed quiescence begins immediately at the tips, and then migrates inward over the following days to the intersection of the cross fault with the M7.1 fault. This migration is consistent with a model in which the delay is due to the unresolved spatial variability (heterogeneity) of the Coulomb stress change (see sketch in Figure 11). Such a variability can arise either (1) due to the variability of the target fault geometries on which the stress is resolved: small faults hosting small earthquakes can have geometries that depart from the SWVF (main M6.4 fault); or (2) directly due to the variability of the tensorial stress change, in particular close to the main fault where unresolved slip heterogeneity would affect the stress change (Helmstetter & Shaw, 2006; Marsan, 2006).

Looking at an area where the Coulomb stress change is heterogeneous but negative on average, the cumulative effect on seismicity will result in a delayed quiescence, the longer the delay as the degree of heterogeneity

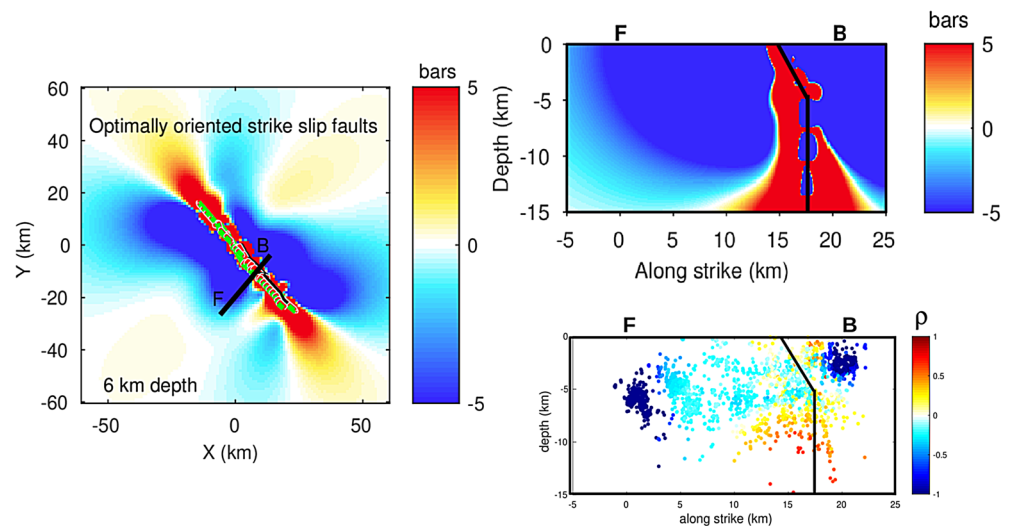


**Figure 9.** Change in Coulomb stress following the M7.1 mainshock. Left: map of Coulomb stress resolved at 6 km depth for vertical, left-lateral strike-slip target faults striking at  $221^\circ$  (similar geometry as the M6.4 cross fault), using the slip model of Ross et al. (2019). Right, top: same as the map, but for the cross section B-F along the cross fault (main fault of the M6.4 mainshock). The intersection of the M7.1 rupture according to the slip model of Ross et al. (2019) is shown in black. Right, bottom: change in seismicity rate in log10 scale ( $\rho$ -value) following the M7.1 mainshock along this section (only earthquakes within 2 km of the section are shown). For each of these earthquakes, the rate change is computed using the  $N = 400$  closest neighbors, see main text.

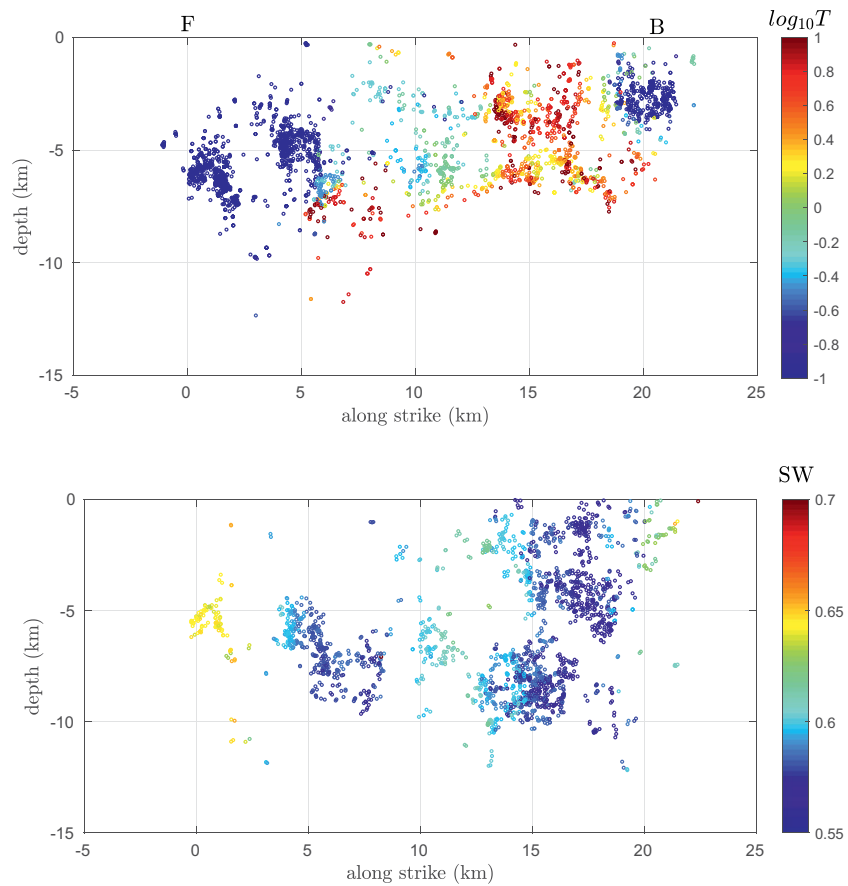


**Figure 10.** (Top) beginning (in days) of the seismic quiescence along the cross fault (transect B-F of Figure 6), in log scale. (Bottom) smoothed waveform similarity coefficient SW of Trugman et al. (2020). We only show earthquakes (i) located within 2 km of the B-F transect, (ii) for the top section: occurring between the M6.4 and the M7.1 mainshock in zones undergoing an observable quiescence in the 0–18.87 days after the M7.1, or (for the bottom graph) occurring after the M6.4 shock. Note that the Trugman et al. (2020) data set differs from the QTM data set of Ross et al. (2019), and that the two sections have different selection criteria. QTM, Quake Template Matching.

increases (Kroll et al., 2017; Toda et al., 2012). With this in mind, delays are expected to be significant where (1) the variability in fault geometries is strong, and (2) near the main M7.1 fault. Feature (1) is likely to be characteristic of the central part where the two main faults intersect. Trugman et al. (2020) found that this area is where most antisimilar earthquake pairs take place (cf. their Figure S7). Such earthquakes have similar waveforms but with opposite polarities, and thus correspond to ruptures accommodating slip in opposite directions on identical faults. This requires both a high level of stress variability at the scale of 100 m or less, and a large local stress drop during the M7.1 rupture so that this highly variable stress change can locally overcome the background stress field. The M6.4 cross-cut fault has a higher waveform similarity coefficient SW at its tips (Trugman et al., 2020), cf. Figure 10. This coefficient measures how similar the waveforms of an earthquake are compared to waveforms of its neighbors. Low SW coefficients are found where structural heterogeneity is strong, which is the case here in the middle section of the SWV fault. Feature (2) will also be found in the central part, that is, near the M7.1 fault.

We thus suggest that the observed inward migration of the quiescence results from unresolved heterogeneous stress change; the heterogeneity becoming weaker as we go toward the tips (locations B and F), the delay becomes shorter, hence a migration. This effect has already been postulated (e.g., Figure 9 of Marsan, 2006) but is here observed for the first time.

Other explanations for delayed quiescences have been proposed in previous studies. One is that dynamic triggering dominates at early times, so that the activity shutdown caused by static stress is only visible at

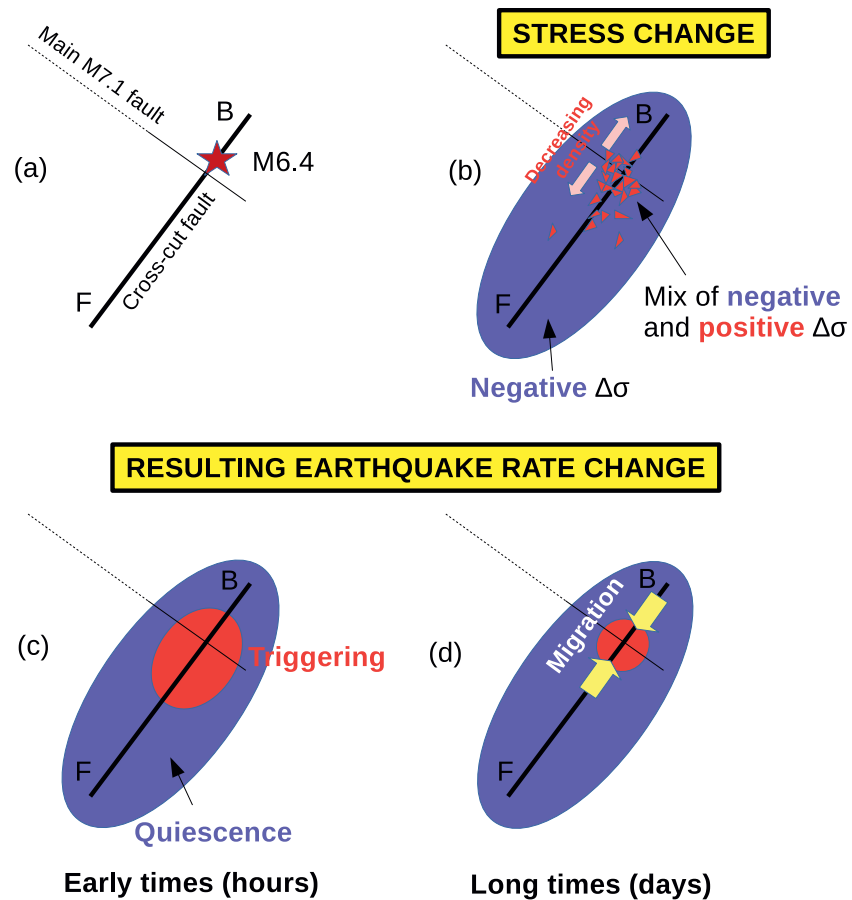


**Figure 11.** (a) General context of the sequence; (b) following the M7.1 rupture, the Coulomb stress change is mostly negative along the M6.4 fault, although in the middle part (intersection of the two faults) the stress change  $\Delta\sigma$  is heterogeneous due to slip and structural heterogeneities. (c) At early times the positive  $\Delta\sigma$  dominate the seismicity rate change, hence initial triggering affects a broad middle part; (d) at longer times quiescence follows the initial triggering where the proportion of positive versus negative  $\Delta\sigma$  is low. This results in an apparent spreading of the quiescence toward the middle (“inward migration”).

longer time scales (Daniel et al, 2006, 2008; Meng & Peng, 2014). Since static stress decays more quickly with distance than dynamic stress, it would be expected that quiescence at remote locations should be delayed by a longer time than closer to the main rupture. Indeed, in this scenario, the duration of the initial triggering phase depends on the absolute value of both the negative static stress change  $\Delta\sigma_s$  and the dynamic stress change  $\Delta\sigma_d$ . For a large  $\Delta\sigma_s$  and a small  $\Delta\sigma_d$ , the dynamically triggered seismicity will be weak and rapidly overcome by the strong shutdown imposed by the static stress change. In the opposite case (small  $\Delta\sigma_s$  and large  $\Delta\sigma_d$ ), the initial triggering phase will last longer. This duration is therefore positively correlated with  $\frac{\Delta\sigma_d}{\Delta\sigma_s}$ , which increases with distance from the mainshock. Since we observe the opposite, that is, the delay before the onset of the quiescence is shorter at the tips of the cross-cut fault, we believe that dynamically triggered activity is not the controlling mechanism for the existence of delayed quiescence during this sequence.

## 5. Conclusions

The succession of the two Ridgecrest mainshocks, as well as triggered creep along the Garlock fault, are well explained by static stress changes (Barnhart et al., 2019; Chen et al., 2020). Complications, however, arise when adding in smaller stress sources. For example, Barnhart et al. (2019) emphasize that aftershocks of the

M6.4 shock have a significant contribution to the change in stress at the hypocenter of the M7.1 shock, but that this contribution is not well constrained given their relative proximity that enhances any errors in the source parameters of the aftershocks. More generally, aftershock activity is mostly controlled by unresolved slip variability, as it occurs on or close to the ruptured fault. Models that couple such variability (modeled in the statistical sense) with friction laws can explain the general dynamics of aftershock sequences (Cattania et al, 2014; Helmstetter & Shaw, 2006; Kroll et al., 2017; Marsan, 2006; Toda et al., 2012), in particular the succession of an initial phase of triggering, followed by seismicity quiescence. The delay with which the quiescence emerges is controlled by the level of stress change heterogeneity.

The Ridgecrest sequence offers a remarkable illustration of this: stress heterogeneity at the intersection of the Salt Wells Valley Fault and the Paxton Ranch Fault cause the seismicity quiescence following the M7.1 mainshock to be delayed by days, giving birth to an apparent inward migration of quiescence along the SWVF. To account for small scale variability in aftershock modeling is challenging and has been up to now done in a statistical way. The emergence of even higher quality earthquake datasets, for example those generated with template matching methods, will offer new ways to address this variability in a more deterministic manner, and help us better understand near-fault aftershock dynamics.

### Data Availability Statement

The QTM data set can be found at <https://scedc.caltech.edu/research-tools/QTM-ridgecrest.html>. The SCSN earthquake catalog is at <https://service.scedc.caltech.edu/eq-catalogs>. The authors used the M7.1 slip model of Ross et al. (2019) which can be accessed at the SRCMOD database <http://equake-rc.info/SRCMOD/searchmodels/viewmodel/S2019RIDGEC02ROSS>. We used the Coulomb 3.4 software of Toda et al. (2011).

### Acknowledgments

This work was funded by the Agence Nationale de la Recherche (ANR-17-CE31-0002-01) AtypicSSE project. The authors thank Yen Joe Tan, Ross Stein, James Hollingsworth for discussions on this work, as well as the Associate Editor and the two anonymous reviewers who helped us improving this manuscript.

### References

- Barnhart, W. D., Hayes, G. P., & Gold, R. D. (2019). The July 2019 Ridgecrest, California, earthquake sequence: Kinematics of slip and stressing in cross-fault ruptures. *Geophysical Research Letters*, *46*(21), 11859–11867.
- Cattania, C., Hainzl, S., Wang, L. F., Roth, F., & Enescu, B. (2014). Propagation of Coulomb stress uncertainties in physics-based aftershock models. *Journal of Geophysical Research: Solid Earth*, *119*(10), 7846–7864. <https://doi.org/10.1002/2014JB011183>
- Chen, K. J., Avouac, J. P., Aati, S., Milliner, C., Zheng, F., & Shi, C. (2020). Cascading and pulse-like ruptures during the 2019 Ridgecrest earthquakes in the Eastern California Shear Zone. *Nature Communications*, *11*(1), 22. <https://doi.org/10.1038/s41467-019-13750-w>
- Daniel, G., Marsan, D., & Bouchon, M. (2006). Perturbation of the Izmit earthquake aftershock decaying activity following the 1999 M-w 7.2 Duzce, Turkey, earthquake. *Journal of Geophysical Research*, *111*(B5), B05310. <https://doi.org/10.1029/2005JB003978>
- Daniel, G., Marsan, D., & Bouchon, M. (2008). Earthquake triggering in southern Iceland following the June 2000 M-s 6.6 doublet. *Journal of Geophysical Research*, *113*(B5), B05310. <https://doi.org/10.1029/2007JB005107>
- Dieterich, J., Cayol, V., & Okubo, P. (2000). The use of earthquake rate changes as a stress meter at Kilauea volcano. *Nature*, *408*(6811), 457–460. <https://doi.org/10.1038/35044054>
- Dieterich, J. H., & Okubo, P. G. (1996). An unusual pattern of recurring seismic quiescence at Kalapana, Hawaii. *Geophysical Research Letters*, *23*(5), 447–450. <https://doi.org/10.1029/96GL00009>
- Du Ross, C. B., Gold, R. D., Dawson, T. E., Scharer, K. M., Kendrick, K. J., Akciz, S. O., et al. (2020). Surface displacement distributions for the July 2019 Ridgecrest, California, Earthquake ruptures. *Bulletin of the Seismological Society of America*, *110*(4), 1400–1418. <https://doi.org/10.1785/0120200058>
- Felzer, K. R., & Brodsky, E. E. (2005). Testing the stress shadow hypothesis. *Journal of Geophysical Research*, *110*(B5), B05S09. <https://doi.org/10.1029/2004JB003277>
- Felzer, K. R., & Brodsky, E. E. (2006). Decay of aftershock density with distance indicates triggering by dynamic stress. *Nature*, *441*(7094), 735–738. <https://doi.org/10.1038/nature04799>
- Green, R. G., Greenfield, T., & White, R. S. (2015). Triggered earthquakes suppressed by an evolving stress shadow from a propagating dyke. *Nature Geoscience*, *8*(8), 629–632. <https://doi.org/10.1038/NNGEO2491>
- Hainzl, S. (2016a). Rate-dependent incompleteness of earthquake catalogs. *Seismological Research Letters*, *87*(2), 337–344. <https://doi.org/10.1785/0220150211>
- Hainzl, S. (2016b). Apparent triggering function of aftershocks resulting from rate-dependent incompleteness of earthquake catalogs. *Journal of Geophysical Research: Solid Earth*, *121*(9), 6499–6509. <https://doi.org/10.1002/2016JB013319>
- Harris, R. A., & Simpson, R. W. (1996). In the shadow of 1857—The effect of the Great Fi Tejon earthquake on subsequent earthquakes in southern California. *Geophysical Research Letters*, *23*(3), 229–232. <https://doi.org/10.1029/96GL00015>
- Harris, R. A., & Simpson, R. W. (1998). Suppression of large earthquakes by stress shadows: A comparison of Coulomb and rate-and-state failure. *Journal of Geophysical Research*, *103*(B10), 24439–24451. <https://doi.org/10.1029/98JB00793>
- Harris, R. A., & Simpson, R. W. (2002). The 1999 M-w 7.1 Hector Mine, California, earthquake: A test of the stress shadow hypothesis?. *Bulletin of the Seismological Society of America*, *92*(4), 1497–1512. <https://doi.org/10.1785/0120000913>
- Helmstetter, A., Kagan, Y. Y., & Jackson, D. D. (2006). Comparison of short-term and time-independent earthquake forecast models for southern California. *Bulletin of the Seismological Society of America*, *96*(1), 90–106. <https://doi.org/10.1785/0120050067>
- Helmstetter, A., & Shaw, B. E. (2006). Relation between stress heterogeneity and aftershock rate in the rate-and-state model. *Journal of Geophysical Research*, *111*(B7), B07304. <https://doi.org/10.1029/2005JB004077>

- Kroll, K. A., Richards-Dinger, K. B., Dieterich, J. H., & Cochran, E. S. (2017). Delayed seismicity rate changes controlled by static stress transfer. *Journal of Geophysical Research: Solid Earth*, *122*(10), 7951–7965. <https://doi.org/10.1002/2017JB014227>
- Liu, C. L., Lay, T., Brodsky, E. E., Dascher-Cousineau, K., & Xiong, X. (2019). Coseismic rupture process of the large 2019 Ridgecrest earthquakes from joint inversion of geodetic and seismological observations. *Geophysical Research Letters*, *46*(21), 11820–11829. <https://doi.org/10.1029/2019GL084949>
- Maccaferri, F., Rivalta, E., Passarelli, L., & Jonsson, S. (2013). The stress shadow induced by the 1975–1984 Krafla rifting episode. *Journal of Geophysical Research: Solid Earth*, *118*(3), 1109–1121. <https://doi.org/10.1002/jgrb.50134>
- Ma, K. F., Chan, C. H., & Stein, R. S. (2005). Response of seismicity to Coulomb stress triggers and shadows of the 1999 M<sub>w</sub>=7.6 Chi-Chi, Taiwan, earthquake. *Journal of Geophysical Research*, *110*(B5), B05S19. <https://doi.org/10.1029/2004JB003389>
- Mallam, E. P., & Zoback, M. D. (2007). Assessing elastic Coulomb stress transfer models using seismicity rates in southern California and southwestern Japan. *Journal of Geophysical Research*, *112*(B3), B03304. <https://doi.org/10.1029/2005JB004076>
- Marsan, D. (2003). Triggering of seismicity at short timescales following Californian earthquakes. *Journal of Geophysical Research*, *108*(B5), 2266. <https://doi.org/10.1029/2002JB001946>
- Marsan, D. (2006). Can coseismic stress variability suppress seismicity shadows? Insights from a rate-and-state friction model. *Journal of Geophysical Research*, *111*(B6), B06305. <https://doi.org/10.1029/2005JB004060>
- Marsan, D., & Daniel, G. (2007). Measuring the heterogeneity of the coseismic stress change following the 1999 M<sub>w</sub>7.6 Chi-Chi earthquake. *Journal of Geophysical Research*, *112*(B7), B07305. <https://doi.org/10.1029/2006JB004651>
- Marsan, D., & Nalbant, S. S. (2005). Methods for measuring seismicity rate changes: A review and a study of how the M<sub>w</sub> 7.3 Landers earthquake affected the aftershock sequence of the M<sub>w</sub> 6.1 Joshua Tree earthquake. *Pure and Applied Geophysics*, *162*(6–7), 1151–1185. <https://doi.org/10.1007/s00024-004-2665-4>
- Meier, M. A., Werner, M. J., Woessner, J., & Wiemer, S. (2014). A search for evidence of secondary static stress triggering during the 1992 M<sub>w</sub>7.3 Landers, California, earthquake sequence. *Journal of Geophysical Research: Solid Earth*, *119*(4), 3354–3370. <https://doi.org/10.1002/2013JB010385>
- Meng, X. F., & Peng, Z. G. (2014). Seismicity rate changes in the Salton Sea geothermal field and the San Jacinto Fault Zone after the 2010 M<sub>w</sub> 7.2 El Mayor-Cucapah earthquake. *Geophysical Journal International*, *197*(3), 1750–1762. <https://doi.org/10.1093/gji/ggu085>
- Meng, X. F., Peng, Z. G., & Hardebeck, J. L. (2013). Seismicity around Parkfield correlates with static shear stress changes following the 2003 M<sub>w</sub>6.5 San Simeon earthquake. *Journal of Geophysical Research: Solid Earth*, *118*(7), 3576–3591. <https://doi.org/10.1002/jgrb.50271>
- Omori (1895). On the aftershocks of earthquakes. *The Journal of the College of Science, Imperial University of Tokyo*, *7*, 111–200.
- Pollitz, F. F., Stein, R. S., Sevilgen, V., & Burgmann, R. (2012). The 11 April 2012 east Indian Ocean earthquake triggered large aftershocks worldwide. *Nature*, *490*(7419), 250–253. <https://doi.org/10.1038/nature11504>
- Rollins, C., Stein, R. S., Lin, G., & Kilb, D. (2019). *The Ridgecrest earthquakes: Torn ground, nested foreshocks, Garlock shocks, and Temblor's forecast*. Temblor. <http://doi.org/10.32858/temblor.039>
- Ross, Z. E., Idini, B., Jia, Z., Stephenson, O. L., Zhong, M., Wang, X., et al. (2019). Hierarchical interlocked orthogonal faulting in the 2019 Ridgecrest earthquake sequence. *Science*, *366*(6463), 346–351. <https://doi.org/10.1126/science.aaz0109>
- Sevilgen, V., Stein, R. S., & Pollitz, F. F. (2012). Stress imparted by the great 2004 Sumatra earthquake shut down transforms and activated rifts up to 400 km away in the Andaman Sea. *Proceedings of the National Academy of Sciences of the United States of America*, *109*(38), 15152–15156. <https://doi.org/10.1073/pnas.1208799109>
- Toda, S., & Stein, R. (2019). *Ridgecrest earthquake shut down cross-fault aftershocks*. Temblor. <http://doi.org/10.32858/temblor.043>
- Toda, S., Stein, R., Sevilgen, V., & Lin, J. (2011). Coulomb 3.3 Graphic-rich deformation and stress-change software for earthquake, tectonic, and volcano research and teaching—User guide. In *U.S. Geological Survey Open-File Report 2011-1060* (p. 63). USGS. Available at <http://pubs.usgs.gov/of/2011/1060/>
- Toda, S., & Stein, R. S. (2002). Response of the San Andreas fault to the 1983 Coalinga-Nunez earthquakes: An application of interaction-based probabilities for Parkfield. *Journal of Geophysical Research*, *107*(B6), 2126. <https://doi.org/10.1029/2001JB000172>
- Toda, S., & Stein, R. S. (2003). Toggling of seismicity by the 1997 Kagoshima earthquake couplet: A demonstration of time-dependent stress transfer. *Journal of Geophysical Research*, *108*(B12), 2567. <https://doi.org/10.1029/2003JB002527>
- Toda, S., Stein, R. S., Beroza, G. C., & Marsan, D. (2012). Aftershocks halted by static stress shadows. *Nature Geoscience*, *5*(6), 410–413. <https://doi.org/10.1038/NCEO1465>
- Trugman, D. T., Ross, Z. E., & Johnson, P. A. (2020). Imaging stress and faulting complexity through earthquake waveform similarity. *Geophysical Research Letters*, *47*(1), e2019GL085888. <https://doi.org/10.1029/2019GL085888>
- Woessner, J., Hauksson, E., Wiemer, S., & Neukomm, S. (2004). The 1997 Kagoshima (Japan) earthquake doublet: A quantitative analysis of aftershock rate changes. *Geophysical Research Letters*, *31*(3), L03605. <https://doi.org/10.1029/2003GL018858>
- Wyss, M., & Wiemer, S. (2000). Change in the probability for earthquakes in southern California due to the Landers magnitude 7.3 earthquake. *Science*, *290*(5495), 1334–1338. <https://doi.org/10.1126/science.290.5495.1334>
- Yoshida, K., & Hasegawa, A. (2018). Sendai-Okura earthquake swarm induced by the 2011 Tohoku-Oki earthquake in the stress shadow of NE Japan: Detailed fault structure and hypocenter migration. *Tectonophysics*, *733*, 132–147. <https://doi.org/10.1016/j.tecto.2017.12.031>